Polarized radio emission unveils the structure of the pre-supernova circumstellar magnetic field and the radio emission in SN1987A

O. Petruk [1,2,3]★ V. Beshley,[1] S. Orlando,[3] F. Bocchino [3] M. Miceli,[4,3] S. Nagataki [5,6] M. Ono,[5,6] S. Loru,[7] A. Pellizzoni[8] and E. Egron [8]

[1]*Institute for Applied Problems in Mechanics and Mathematics, Naukova Street 3-b, 79060 Lviv, Ukraine*
[2]*Astronomical observatory, Ivan Franko National University of Lviv, Kyryla i Methodia St. 8, UA-79005 Lviv, Ukraine*
[3]*INAF - Osservatorio Astronomico di Palermo, Piazza del Parlamento 1, I-90134 Palermo, Italy*
[4]*Dip. di Fisica e Chimica, Università degli Studi di Palermo, Piazza del Parlamento 1, I-90134 Palermo, Italy*
[5]*Astrophysical Big Bang Laboratory, RIKEN Cluster for Pioneering Research, 2-1 Hirosawa, Wako, Saitama 351-0198, Japan*
[6]*RIKEN Interdisciplinary Theoretical & Mathematical Science Program (iTHEMS), 2-1 Hirosawa, Wako, Saitama 351-0198, Japan*
[7]*INAF - Osservatorio Astrofisico di Catania, Via Santa Sofia 78, I-95123 Catania, Italy*
[8]*INAF - Osservatorio Astronomico di Cagliari, Via della Scienza 5, I-09047 Selargius, Italy*

ABSTRACT

The detected polarized radio emission from the remnant of SN1987A opens the possibility to unveil the structure of the pre-supernova (pre-SN) magnetic field (MF) in the circumstellar medium. Properties derived from direct measurements would be of importance for understanding the progenitor stars and their MFs. As the first step to this goal, we adopted the hydrodynamic (HD) data from an elaborated three-dimensional (3D) numerical model of SN1987A. We have developed an approximate method for 'reconstruction' of 3D MF structure inside SN remnant on the 'HD background'. This method uses the distribution of the MF around the progenitor as the initial condition. With such a 3D magnetohydrodynamic model, we have synthesized the polarization maps for a number of SN1987A models and compared them to the observations. In this way, we have tested different initial configurations of the MF as well as a structure of the synchrotron emission in SN987A. We have recovered the observed polarization pattern and we have found that the radial component of the ambient pre-SN MF should be dominant on the length-scale of the present-day radius of SN1987A. The physical reasons for such a field are discussed.

Key words: MHD – polarization – shock waves – ISM: supernova remnants – magnetic field.

1 INTRODUCTION

Remnant of supernova (SN) 1987A is an attractive object for studies (e.g. McCray & Fransson 2016), for instance: to investigate how the structure and morphology of supernova remnants (SNRs) reflect the properties of the parent SN explosions and the nature of the progenitor stars, to unveil how dust forms after SN explosions, to reconstruct the pre-SN circumstellar medium (CSM) and stellar magnetic field (MF) formed in the latest phases of progenitor star evolution, to understand the spatial distribution of emitting relativistic particles inside SNR. In fact, SN 1987A is the only SN exploded so close to us after the invention of the telescope. It is accurately monitored since the explosion event. Observations span from radio (e.g. Zanardo et al. 2010, 2013; Callingham et al. 2016; Abellán et al. 2017; Cendes et al. 2018) through the optic and infrared bands (e.g. France et al. 2010; Fransson et al. 2015; Larsson et al. 2016; Arendt et al. 2020; Kangas et al. 2022) to X-rays (e.g. Park et al. 2011; Helder et al. 2013; Frank et al. 2016; Miceli et al. 2019; Ravi et al. 2021; Sun et al. 2021; Greco et al. 2021, 2022) and contain a wealth of information about the stellar ejecta, remnant and physics inside.

High-performance three-dimensional (3D) simulations aim to restore the explosion (Alp et al. 2019; Ono et al. 2020), as well as the structure and expansion of SN1987A including spectral variations and detailed morphology of the remnant and ejecta, in particular in X-rays (Orlando et al. 2015, 2020) and in the radio band (Potter et al. 2014; Orlando et al. 2019). The later paper reports the first 3D magnetohydrodynamic (MHD) numerical simulations of the remnant of SN1987A.

Important new milestone in observations of SN1987A is detection of the polarized radio emission (Zanardo et al. 2018). For the first time, it allows one to test models of MF in this SNR. One of the most distinctive features apparent from this observational result is the dominant radial orientation of the MF vectors. This is in line with what is found in other young SNRs (Dickel & Milne 1976; Dubner & Giacani 2015).

The MF structure inside SNR and thus the polarization pattern depend on MF configuration in and around a progenitor in the pre-explosion era, on its behaviour during the development of the explosion and on properties of its evolution from the shock breakout to the evolved SNR. Synthesis of polarization images essentially require knowledge of the internal 3D morphology of MF in SNR. Thus, the full 3D MHD simulations are required in order to produce synthetic polarization maps. The ideal simulations reproduce subsequently as SN event as development of the remnant

in three dimensions. This is a quite demanding task because the evolution covers many orders in time (from microseconds to thousand years) and space (from astronomical unit to few parsecs). Therefore, a viable approach could consist in the two phases: (i) simulations of an SN event, (ii) simulations of an SN remnant with the outcome from the previous step as initial conditions.

Though the MHD studies as SNe as SNRs were initiated few decades ago (e.g. LeBlanc & Wilson 1970; Falle 1975), the explorations of 3D MHD models is quite new field. There are two directions in MHD studies of SN explosions (see an overview by Reichert et al. 2022). Namely, the magnetorotational core-collapse SNe (Mösta et al. 2015; Obergaulinger, Just & Aloy 2018; Kuroda et al. 2020; Obergaulinger & Aloy 2020, 2021; Aloy & Obergaulinger 2021) and neutrino-driven core-collapse SN explosions of non-rotating stars (Müller & Varma 2020; Matsumoto et al. 2022; Varma, Mueller & Schneider 2022). It is shown in particular that MF provides a crucial support for development of explosions in both these types of models and the probability to explode lowers for models with low MF.

We have studied the role and behaviour of MF during different phases of SNR evolution (Petruk, Kuzyo & Beshley 2016; Petruk et al. 2018, 2021) and have shown that MF is dynamically important in SNRs only in the post-adiabatic epochs. It is obvious, however, that the synchrotron images and polarization patterns depend on the structure of MF inside SNR at any evolutionary stage (e.g. Orlando et al. 2007; Petruk et al. 2017).

In our paper, we would like to get hints about the preexplosion MF from observations of polarization of SN1987A. Such constraints cast light on the relatively uncertain models of the evolution of massive stars, their explosions and SNRs. Determination of the pre-SN MF configuration of the progenitor star is important to obtain information, in general, on the latest phases of evolution of massive stars and, for this particular case, to obtain information on the evolution of a binary system evolving through a common-envelope phase as suggested by some authors (e.g. Morris & Podsiadlowski 2007).

Up to now, there is no MHD model for the explosion of SN1987A. Therefore, an ad hoc configuration of MF was introduced in the MHD model for the remnant of this SN (Orlando et al. 2019). In Section 2 of this paper, we analyse the polarization patterns as they appear in this model.

In order to check different ideas about initial MF configuration and explore the parameter space, one needs to run massive 3D MHD simulations for each eventual MF model and parameter set. Such simulations are quite demanding because they should be performed in the highest possible resolution. In this paper, we adopt a different approach. The existing hydrodynamic (HD) model of SN1987A (Orlando et al. 2015, 2019, 2020) agrees well with a wealth of observational information. Therefore, a method for reconstruction of MF structure inside SNR on top of the known 3D HD background would be useful because it allows one to test a given MF model by comparison of synthetic polarized images with the observations without massive 3D simulations. The details of such an approximate approach are described in Section 3, where we also test the method and show its limitations. The method is applied to SN1987A and results are discussed in Section 4.

2 POLARIZATION MAPS OF SN1987A FROM THE NUMERICAL MHD MODEL

2.1 Observed polarization and our approach

The radio emission from SN1987A is monitored since the very beginning of the remnant evolution. The polarized intensity is a minor fraction of the total intensity. The later grows with time (Zanardo et al. 2010) and the polarized intensity – being a fraction of the total – is expected to grow as well. In fact, the polarized radio emission from SN1987A was detected, for the first, time with Australia Telescope Compact Array (Zanardo et al. 2018). Fig. 3 in this reference reports the image at 22 GHz which is of interest for our study. The rotation measure in SN987A is compatible with zero at this frequency (fig. 2 in Zanardo et al. 2018) and the pattern of polarization vectors shows the MF directions unchanged by the Faraday effect. Error in the polarization angles is reported to be less than 5 per cent.

The first 3D MHD model of SN1987A as a result of self-consistent massive numerical simulations was reported by Orlando et al. (2019). The model of SN used as initial conditions for the SNR evolution was 1D; it was remapped in the 3D domain in a spherically symmetric way. In the following study (Orlando et al. 2020), the model was elaborated in order to include the ejecta asymmetry derived in dedicated 3D simulations of the core-collapse SN explosion (Ono et al. 2020).

In this section, we use the model MOD-B1 (described in section 2.1 in Orlando et al. 2019). It assumes the MF configuration to be the common Parker (1958) spiral

$$B_{\rm r} = \frac{A_1}{r^2}, \qquad B_{\phi} = -\frac{A_2}{r}\sin\theta, \qquad (1)$$

with

$$A_1 = B_0 r_0^2, \qquad A_2 = B_0 r_0^2 \omega_{\rm s}/u_{\rm w}, \qquad (2)$$

where B_0 is the MF strength at the surface of the star, r_0 its radius, $\omega_{\rm s}$ the angular velocity of the stellar rotation, $u_{\rm w}$ is the speed of wind, $\theta = \pi/2$ in the equatorial plane. Numerically, the parameters $A_1 = 3 \times 10^{28}$ G cm^2, $A_2 = 8 \times 10^{10}$ G cm were used for the MOD-B1 model (see visualization of the initial MF configuration on fig. 1 in Orlando et al. 2019).

Numerical simulations reported by Orlando et al. (2019) were performed on a grid with 1024^3 zones. The data cubes were downgraded to the matrices of the size 256^3 for image analysis in this paper. Such resolution shortens time for production of the polarization maps while keeping all its features. In this paper, we use the data for year 30 of SN1987A evolution which corresponds to epoch observed by ATCA (Zanardo et al. 2018). Images of the SNR projection on the plane of the sky which we derive correspond to the frequency 22 GHz and are smoothed to match the resolution of the observations.

Sugerman et al. (2005) found that the structures in and around SN1987A are inclined in respect to the fixed Cartesian coordinate system (*x*-axis to the west, *y*-axis to the north, and *z*-axis toward the observer) on angles 41º with axis *x* (i.e. the upper side of the dense ring is closer to the observer[1]), −8º with the axis *y* (i.e. the right side closer to the observer) and −9º with the axis *z* (the left part up). In order to reach such an orientation, we follow Potter et al. (2014, see also their fig. 1) and perform successive *x*–*y*–*z* rotations of our MHD datacubes around respective axes on angles $i_{\rm x} = -49º$ (the ring plane is horizontal initially in our simulations), $i_{\rm y} = -5º$, and $i_{\rm z} = -3º$.

The synthesis of polarization maps is based on a method developed by Bandiera & Petruk (2016) and Petruk et al. (2017). It includes an important effect of the Faraday rotation of the polarization planes along the line of sight in the SNR interior as well as prescription

---

[1]In this reference, the plane of the equatorial ring was considered initially to be vertical, i.e. to coincide with the *xy* plane, with the major axis of ellipse along the *x*-axis.

of the turbulent MF evolution downstream of the shock. We would like to note that we account completely for the complex internal structures of density and MF inside SNR while calculating the rotation of the polarization planes. In this paper, we adopt this method for synthesis of the Stokes-parameters maps for young SNR in medium with non-uniform distribution of density and MF (details of calculations of the radio emissivity are given in Orlando et al. 2007, 2019). Electrons are assumed to be injected independently of the shock obliquity (this is not a limitation of our model because MF has nearly the same obliquity everywhere in the emitting 'barrel' of SN1987A), accelerated on the forward shock and evolved downstream according to the HD structure of SNR. The energy spectrum of the radio-emitting electrons is taken to be power law. We adopt the radio spectral index $\alpha = 0.7$ (Zanardo et al. 2010) for our images.

The evolution of the radio flux from the model MOD-B1 agrees with the observed light curve if relativistic electrons are provided by the forward shock only (fig. 8 in Orlando et al. 2019). Therefore, we do not consider the particle acceleration at the reverse shock of SN1987A. In fact, we exclude from the image synthesis the cells where ≥ 10 per cent of the material is ejecta (the number 10 per cent is not fine tuned; in fact any number up to $\simeq 60$ per cent produce almost the same results because the contact discontinuity transition is rather sharp). Reasons for a minor contribution or suppression of the radio emission from the reverse shock in SN1987A are considered in details by Orlando et al. (2019). Similar effect is found in SN1993J where the high absorption of the radio emission by the ejecta is observed with the ejecta opacity close to 100 per cent (Martí-Vidal et al. 2011).

In this paper, we neglect the turbulent component of MF assuming that the observed polarization pattern is dominated by the ordered component MF. Turbulent MF if randomly oriented everywhere in the SNR interior should not alter the global MF structure which is sampled by the polarization images. Such assumption is in agreement with the observed polarization planes in SN1987A which look quite ordered. It also simplifies considerably production of the polarization direction map that is the main goal toward understanding the global MF structure in SNR. However, this simplification prevents us from producing the polarization fraction map which is sensitive to the MF randomness. We will use an approximate tool in order to estimate the ratio of the random δB to the ordered B MF components in SN1987A.

The number of particles injected and accelerated at the shock expanding into the non-uniform medium – and therefore the normalization of the momentum spectrum of the radio-emitting electrons κ – is generally considered proportional to the pre-shock number density n_o (Orlando et al. 2007). For references, the number densities in the structures surrounded the SN progenitor are: H II region 90 cm^{-3}, equatorial ring 1000 cm^{-3}, dense clumps in the ring 2.5×10^4 cm^{-3} on average (see table 1 in Orlando et al. 2019 and fig. 1 in Orlando et al. 2015).

Multiwavelength observations of SN1987A prove the shock passage through the equatorial ring and interactions with clumps during recent decades [e.g. in optical (Gröningsson et al. 2008; Fransson et al. 2015) and X-ray (Maggi et al. 2012; Helder et al. 2013) photons]. Recent observations even show that the shock has already left the outer edge of the ring (Frank et al. (2016), Sun et al. (2021), Ravi et al. (2021) in the X-ray band; Cendes et al. (2018) in the radio band; Larsson et al. (2019) in the optical band). The period of SNR interaction with the ring is clearly visible in the thermal X-rays: the light curve and the spectrum are dominated since year 14 after the explosion by the emission from the material of the ring (Orlando et al. 2015, 2019, 2020). In particular, the bump in the X-ray light

curve in fig. 5 in Orlando et al. (2019) is proved to be due to the illuminated ring material (the dash–dotted line on the figure).

In contrast, the evolution of the radio flux does not exhibit a bump in the radio light curve (fig. 5 in Zanardo et al. 2010 or fig. 7 in Orlando et al. 2019). Therefore, it could be that the dense ring does not contribute much to the radio light curve. Similar conclusion could follow from analysis of Potter et al. (2014): The discrepancy is evident between the evolution of the observed radio emission and the synthesized one from the HD model. The differences which eventually could be due to the same reason are visible from the X-ray and radio images. The brightest regions in the sequence of the X-ray images in the years 2000–2016 seems to be dominated by the dense clumps (fig. 5 in Frank et al. 2016) and an inversion of the east/west asymmetry into the west/east one is evident during these years (fig. 6 in the same reference). In contrast, the sequence of the radio images (fig. 1 in Cendes et al. 2018) has the brightness maximum always at the East during the whole this period. This difference between the radio and X-ray images is also well demonstrated at fig. 1 by Indebetouw et al. (2014) for the years 2011–2012. Again, it seems that the very dense material of the ring and clumps does not manifest itself in the radio band (maybe due to a rapid decrease of injection or acceleration efficiencies, for example, in portions of the shock which rapidly decelerate in the high-density environment and quickly become radiative).

Another result also supports the scenario that no significant radio emission originates from the ring. The analysis in the Fourier space by (Ng et al. 2008, 2013) shows that the geometrical shape of the radio morphology of SN1987A can be a thick torus. In fact, the toy model of a thick torus adopted by these authors fits well in describing the emission originating from the H II region without the need to invoke emission from the shocked ring.

In view of these points, we consider the two alternatives in this paper. Namely, the *alternative A* keeps the proportionality $\kappa \propto n_o$ everywhere. The *alternative B* excludes the material of the ring and clumps in calculation of κ if the fraction of the ring material in a cell is between 0.3 and 1 and the number density >1000 cm^{-3}. Note that this material is present in all other aspects of the model, for example, in calculation of the internal Faraday rotation. The distributions of the emitting electron density in both these alternatives are shown in Fig. 1.

2.2 Polarization images for the existing MHD model

The synthesized images of the total I and the polarized intensity I_{pol} for the model MOD-B1 from Orlando et al. (2019) are shown in Fig. 2 for the *alternative A* and on Fig. 3 for the *alternative B*. The map of the Stokes parameter I on our Fig. 3 (left-hand panel) corresponds to fig. 9 by Orlando et al. (2019) but the age, frequency, and convolution differ. In this paper, the modelled images of polarized synchrotron emission from SN1987A are reported for the first time.

The following statements are evident.

(i) Brightness in the *alternative A* is affected by the location of the clumps. They should effectively influence the radio light curve if they contribute to relativistic electrons.

(ii) Radio emission arises in physically different regions of SNR in the two alternatives. The dense ring is dominant in the *alternative A* and it should affect the light curve as well. The image in the *alternative B* is mostly from the shocked H II material and the emitting material is shaped like a barrel.
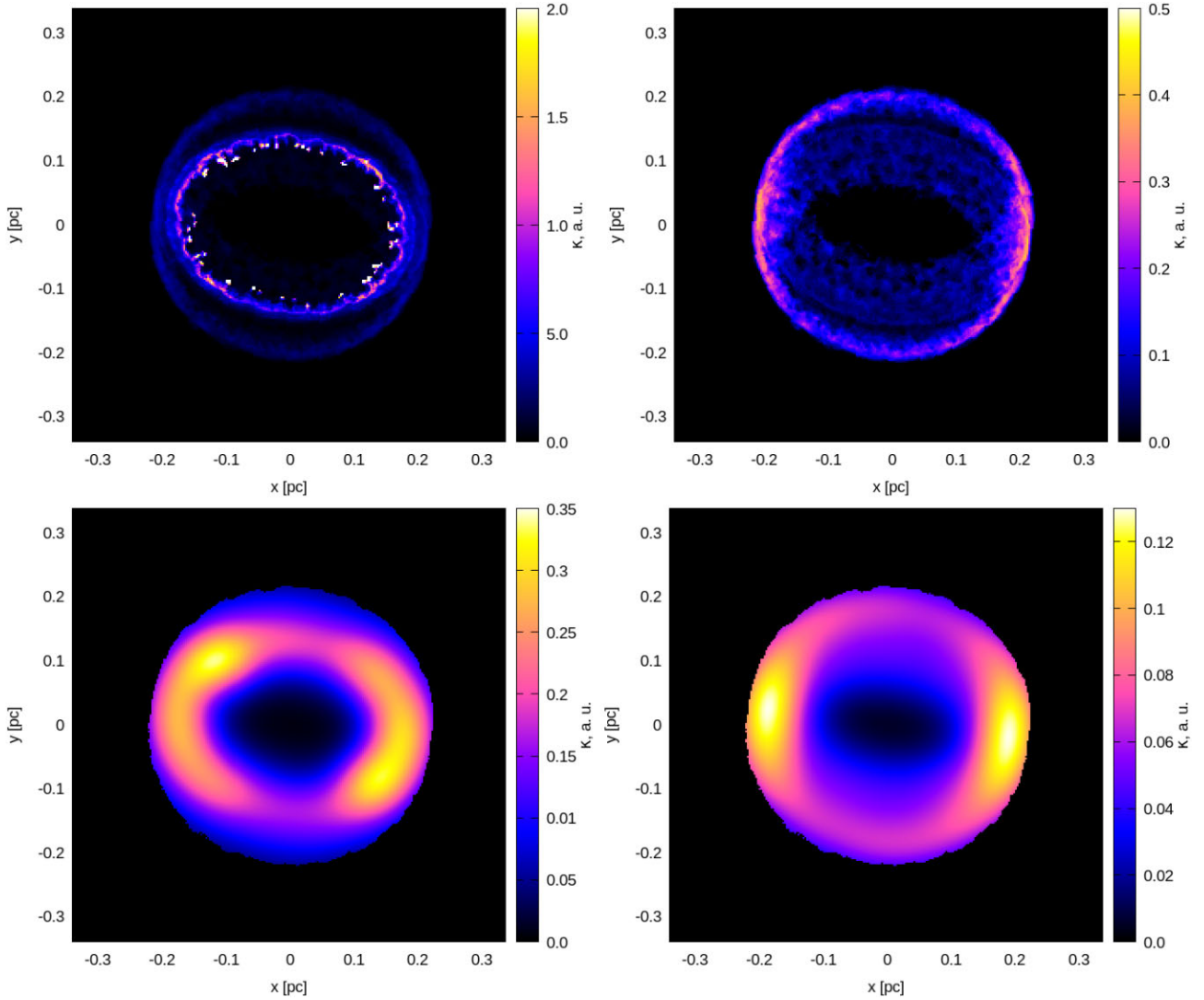
Figure 1. Spatial distribution of the radio-emitting electrons in the two alternatives considered in this paper. These are the maps of the κ integrated along the line of sight (the local synchrotron emissivity is proportional to $\kappa B^{\alpha + 1}$). Left-hand panel: *alternative A*, including the ring and the clump structures. Right-hand panel: *alternative B*, without these dense components. Upper panels: in full resolution, lower panels: smoothed to the resolution of the radio observations.

(iii) These differences are evident from the synthesized images in full resolution. However, there is no clear way to distinguish between the two alternatives from observations because of insufficient instrumental resolution.

(iv) The shape of the image in the *alternative A* is more elliptical compared to the *alternative B*.

(v) The tangential pattern dominates in the distributions of the polarization vectors on Figs 2 and 3. Observed polarization in SN1987A (Zanardo et al. 2018) is more radial than it is in the MOD-B1 model. This conclusion is valid for the both alternatives for κ.

(vi) Therefore, it is evident that the MOD-B1 model does not reproduce the observed polarization map (reported on fig. 3 in Zanardo et al. 2018). Thus, MF in SN1987A has structure different from that adopted in this model.

(vii) Orlando et al. (2019) has also reported numerical MHD simulations for another model, MOD-B100. It was shown that this model does not reproduce the radio light curve. In addition, it has higher tangential MF component ($A_2 = 8 \times 10^{13}$ G cm) comparing

to MOD-B1 and therefore does not correspond to the observed polarization.

It has to be pointed out that the configuration of the MF is important for polarization maps, but not for changing the overall dynamics of the SNR which would be analogous even with a configuration of MF which is different from that adopted in our previous models MOD-B1 and MOD-B100.

In order to check how lower or higher MF strengths or electron density affect the polarisation patterns due to the Faraday effect, we multiplied artificially the rotation measure *RM* by the same factor everywhere in the SNR interior. The images for different factors in the range 0.3–3 are indistinguishable. Though the internal Faraday rotation could change the polarization pattern, it is ineffective for the high frequency of available observations, $\nu = 22$ GHz, because $RM \propto \nu^{-2}$. The polarization observations at lower frequencies which are sensitive to the Faraday effect would be of a considerable importance for testing the models of MF in SN1987A.
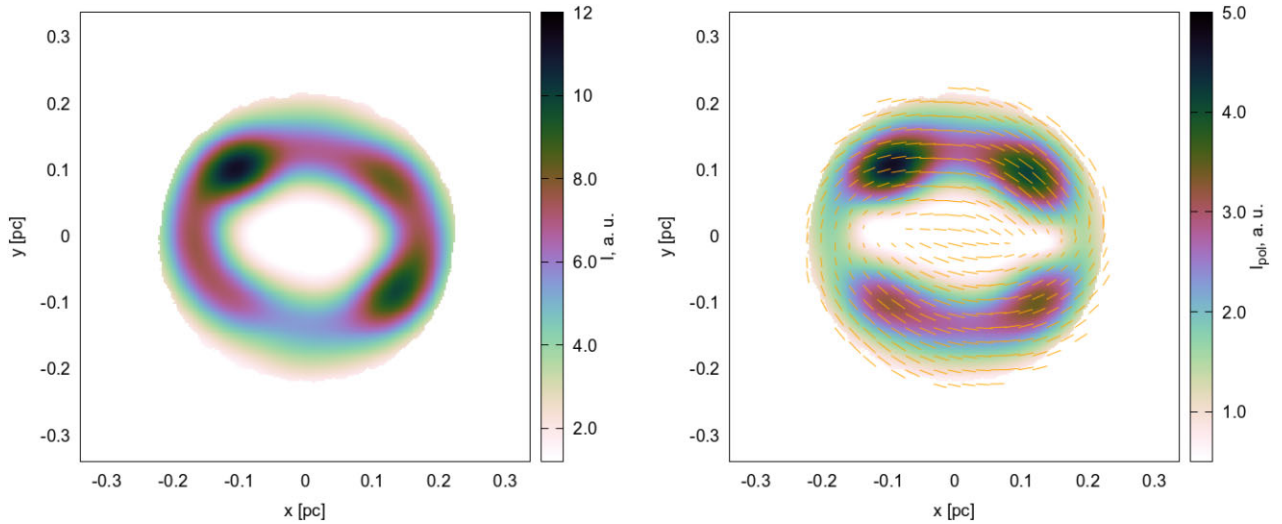
Figure 2. Maps of the Stokes parameter *I* (left-hand panel) and I_{pol} (right-hand panel) for the model MOD-B1 and for the *alternative A*. Polarization vectors corresponds to MF orientation and are proportional to the polarization fraction. Hereafter, our images correspond to year 30 of SNR evolution, to the frequency 22 GHz and are convolved with Gaussian with FWHM = 0″.4. Arbitrary units in colour scales are the same on Figs 2 and 3 in order to make it possible to compare the images one to another.
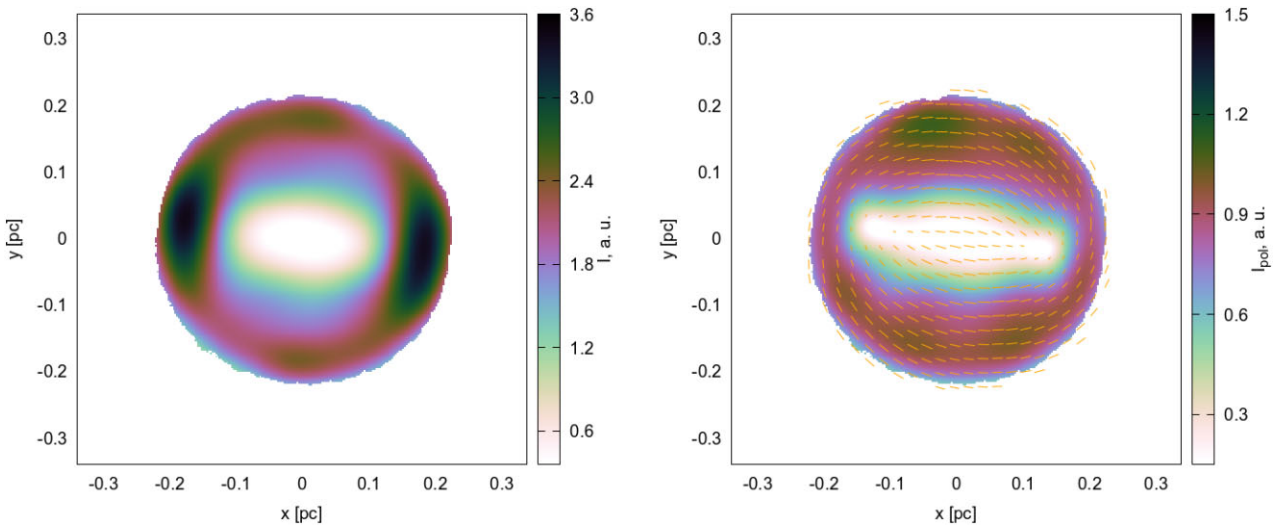

Figure 3. The same as on Fig. 2 for the for the *alternative B* (without contribution of the ring and clumps to the number density of relativistic electrons).

3 METHOD FOR MAGNETIC FIELD RECONSTRUCTION IN HD SIMULATIONS

HD model of SN1987A by Orlando et al. (2019) agree with wealth of observational data. However, as we have just seen, the structure of MF in this model has higher tangential component comparing to the polarization pattern observed in SN1987A. Therefore, there is a need to look for a MF structure which agree with the radio polarization. The full-scale three-dimensional MHD simulations are not suitable for exploring the parameter space. Therefore, we have developed a semi-analytical approximate method which helps us to 'reconstruct' MF structure of evolved SNR once its HD structure is known and a model of initial MF around the SN progenitor before the explosion is assumed. Considering different models of the initial MF, we may find the polarization configuration which resembles the observed pattern.

3.1 Description of the method

Generally, MF pressure in SNRs is considerably smaller than the thermal or ram pressure. SN1987A is not an exception. In the model MOD-B1, for example, the ratio of the thermal to magnetic pressure $\beta > 10^5$ at its forward shock at the time of its breakout of the stellar surface. HD properties of SN1987A are such that MF at the stellar surface has to be >1 MG in order to affect the overall dynamics of this object. This is far above the values allowed by the radio light curves (Orlando et al. 2019).

Considering the limit of the large plasma β (i.e. dynamically unimportant MF), one can use HD numerical simulations in order to prescribe the distribution of MF it should be inside a shell-like SNR.

Let the (non-uniform) distribution of MF in the ambient medium before the SN event $\boldsymbol{B}_o(\boldsymbol{r})$ be known (actually, this is the MF model to be tested). In order to recover MF in an element of plasma at

time t after explosion, we consider its evolution in this element, in Lagrangian approach.

At the beginning, we need to know what was MF in this element at the time t_i when it was shocked. The vector $\boldsymbol{B}_o$ is split to the two components, the parallel and perpendicular ones $B_{\parallel o} = B_o \cos \Theta_o$, $B_{\perp o} = B_o \sin \Theta_o$ where Θ_o is the obliquity angle, i.e. the angle between $\boldsymbol{B}_o$ and the shock normal $\boldsymbol{n}$, index 'o' marks the pre-shock values. If the shock compression ratio is σ then the post-shock components are respectively $B_{\parallel s} = B_{\parallel o}$, $B_{\perp s} = \sigma B_{\perp o}$; they lie in the plane fixed by the vectors $\boldsymbol{B}_o$ and $\boldsymbol{n}$.

At any time moment, the obliquity angle in each 'shocked' cell may be calculated assuming that the portion of the shock located at $\boldsymbol{r}$ at a time moment t_i runs approximately in the radial direction:

$$\cos \Theta_o(\boldsymbol{a}, t_i) = \frac{(\boldsymbol{B}_o(\boldsymbol{a}) \cdot \boldsymbol{a})}{|B_o||a|}, \qquad (3)$$

where $\boldsymbol{a} \equiv \boldsymbol{R}(t_i)$ is the Lagrangian coordinate of a given gas element, $\boldsymbol{R}$ the radius-vector of the shock element. Note, that the three components of the Lagrangian coordinate $\boldsymbol{a}$ should be kept during the simulations in respective tracers; this allows one to convert $\boldsymbol{r}$ to $\boldsymbol{a}$ and vice versa for any time moment t.

A more sophisticated approach could be developed, namely, that the normal $\boldsymbol{n}$ may not be taken in the radial direction for a moment of time t_i but parallel to the shock velocity $\boldsymbol{V}$. It could be somehow more accurate than the approximation of the instant radial expansion because it closely follows the paths of the shock elements (respective numerical simulations should include three additional passive tracers to store the components of the shock velocity vectors). It should be noted, however, that the velocity of the shock in a non-uniform medium is not always perpendicular to the shock surface. Therefore, such approach would also be approximate. The approximation of the radial expansion is simpler and quite accurate for the regions of ambient medium without strong small-scale density gradients which could change considerably the motion direction of a given portion of the shock.

Magnetic flux through co-moving surface ds is constant in an ideal MHD, i.e. $B_\parallel ds_\parallel = \text{const}$, $B_\perp ds_\perp = \text{const}$. Therefore,

$$B_{\parallel s}(a, t_i)a^2 = B_\parallel(a, t)r^2, \qquad B_{\perp s}(a, t_i)a\,da = B_\perp(a, t)r\,dr. \qquad (4)$$

With the use of the continuity equation $\rho_s(a, t_i)a^2 da = \rho(a, t)r^2 dr$, we derive the expressions:

$$B_\parallel(a, t) = B_{\parallel o}(a)\left(\frac{a}{r}\right)^2, \qquad B_\perp(a, t) = B_{\perp o}(a)\frac{\rho(a, t)}{\rho_o(a)}\frac{r}{a}. \qquad (5)$$

The formulae for the conversion of $B_\parallel(a, t)$ and $B_\perp(a, t)$ into the three components of $\boldsymbol{B}(r, t)$ are given by Petruk et al. (2017, Appendix A).

Thus, the 3D structure of $\boldsymbol{B}(r)$ inside SNR depends on the initial model of the ambient field $\boldsymbol{B}_o(r)$, on the initial ambient density distribution $\rho_o(r)$ and on the actual density structure $\rho(r)$ inside SNR. Therefore, introducing ideas for possible distributions of the pre-SN MF $\boldsymbol{B}_o(r)$, one can forecast how would MF $\boldsymbol{B}(r)$ be distributed on-top the 3D HD structure of evolved SNR.

Such quasi-MHD model of SNR (3D data-cubes for HD parameters from the full-scale numerical simulations plus semi-analytically reconstructed data-cubes for MF vectors) may be used to simulate polarization images. These images may then be compared to respective observations. This receipt allows for rather quick tests of different initial MF configurations $\boldsymbol{B}_o(r)$ in cases when the HD structure of SNR known. Once a model for $\boldsymbol{B}_o(r)$ which resembles observations is known from this method, then the full-scale MHD simulations may be performed with this

initial ambient MF in order to study details of MHD evolution of SNR.

In this paper, we use this approximate method to realize hints about the MF and the radio emission structures in SN1987A.

3.2 Test of the method

First, we have tested our method on the Sedov SNR by comparing reconstructed MF with MHD simulations for the Sedov (1959) problem. The reconstructed MF is practically the same as in the 3D MHD simulations of the Sedov SNR. The reason for such accuracy is that our method corresponds to the exact analytical solution for MF profiles downstream of the strong one-dimensional shock from a point explosion in a perfectly conducting gas with weak MF (Korobeinikov 1964).

Then, we have performed the test of the method with the numerical data for MOD-B1 model by Orlando et al. (2019). Fig. 4 compares MF which contribute to the synchrotron emission, namely, the component perpendicular to the line of sight of MF overtaken by the forward shock. Data from the MOD-B1 numerical model of SN1987A is shown on the left-hand side and for the MF reconstructed with our method (with the use of HD data from the same numerical model and with the same $\boldsymbol{B}_o(r)$) is shown in the right-hand side. We see good correspondence of both MF patterns.

In summary, the proposed method is adequate even for rather complicate cases like SN1987A if the general MF morphology is of interest.

4 RESULTS AND DISCUSSION

4.1 Morphology of the synchrotron emission

We have used the approximate approach described in Section 3 in order to find an initial MF configuration which results in the polarization image of SN1987A similar to the observational one reported by Zanardo et al. (2018, fig. 3).

We applied the method to HD data from the numerical model presented by Orlando et al. (2019). Fig. 5 shows the resulting images for the initial MF given by the equations (1)–(2) with the same A_1 as in the model MOD-B1 but with a considerably smaller $A_2 = 2 \times 10^9$ G cm. Such MF results in a required pattern of polarization vectors. Therefore, the stellar rotation ω_s was slower and/or the wind speed u_w was faster before the SN1987A explosion compared to what was assumed in the MOD-B1 model.

The pattern of the polarization vectors is recovered in our images, in both alternatives for the distribution of the radio-emitting electrons. However, the brightness distribution (both total and polarized) is symmetric on our case, contrary to the observations where the left limb is brighter than the right one (Zanardo et al. 2018, fig. 3). This is not surprising because (i) the configuration of the CSM in the considered numerical model is symmetric (except of the clump locations which are random); (ii) the SN explosion was assumed to be spherically symmetric; and (iii) the Parker (1958) formulae describe the symmetric circumstellar MF configuration.

At this point, we do not discuss the nature of the asymmetry but instead perform a simple procedure. Namely, In order to recover the east–west asymmetry in SN1987A image, we have added artificially a gradient of the emissivity by multiplying the 'local' values of the Stokes parameters I, Q, U in each cell of the rotated 3D cube by a factor $\exp(-x/H)$ with x the Cartesian coordinate and $H = 0.5$ pc the length-scale (to be compared to the radius of SN1987A 0.23 pc).
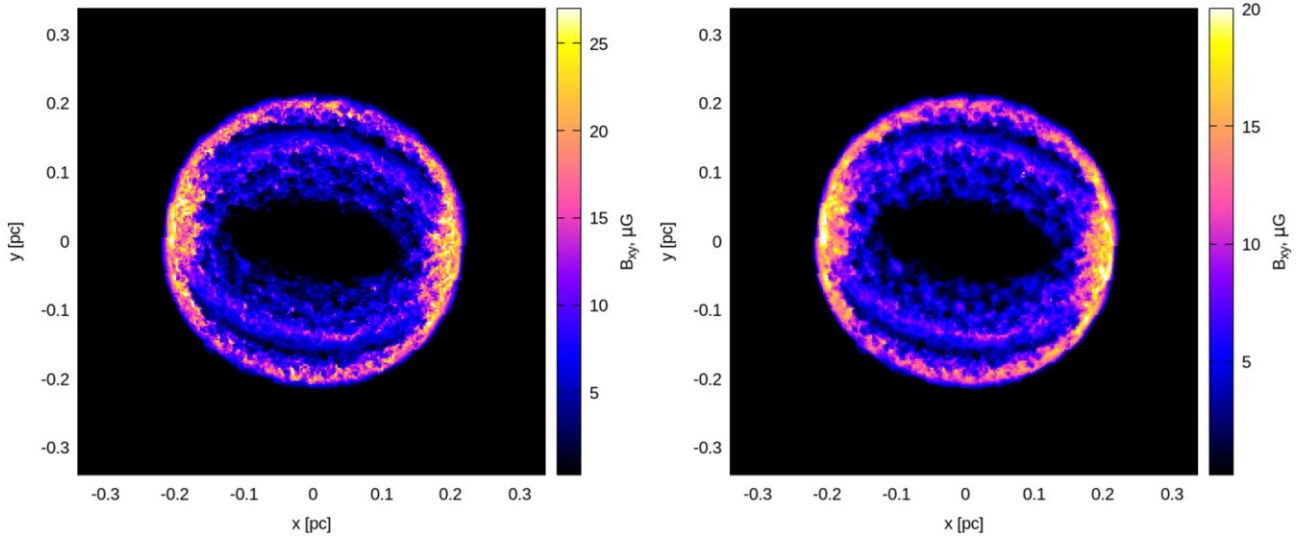
Figure 4. Sum along the line of sight of the MF component perpendicular to the line of sight. Left-hand panel: MF from 3D MHD simulations. Right-hand panel: MF reconstructed from 3D HD data. Note, that these are the MF maps and no distribution of emitting electrons is needed to produce them: MF structure is the same as for *alternative A* and for *alternative B*. Though the absolute values on the colour scales are a bit different, the contrasts between the maximum (27 μG on the left-hand panel, 20 μG on the right-hand panel) and the minimum values are the same on both colour-scales. In other words, the colour-scales differ by a factor only. We have chosen to shift one colour-scale on a factor versus the another one in order to emphasize similarities and to make it more suitable to see correlations between the two images. The ratios of brightness between pixels are more important for comparison of images than the difference on the same factor in the overall amplitude.
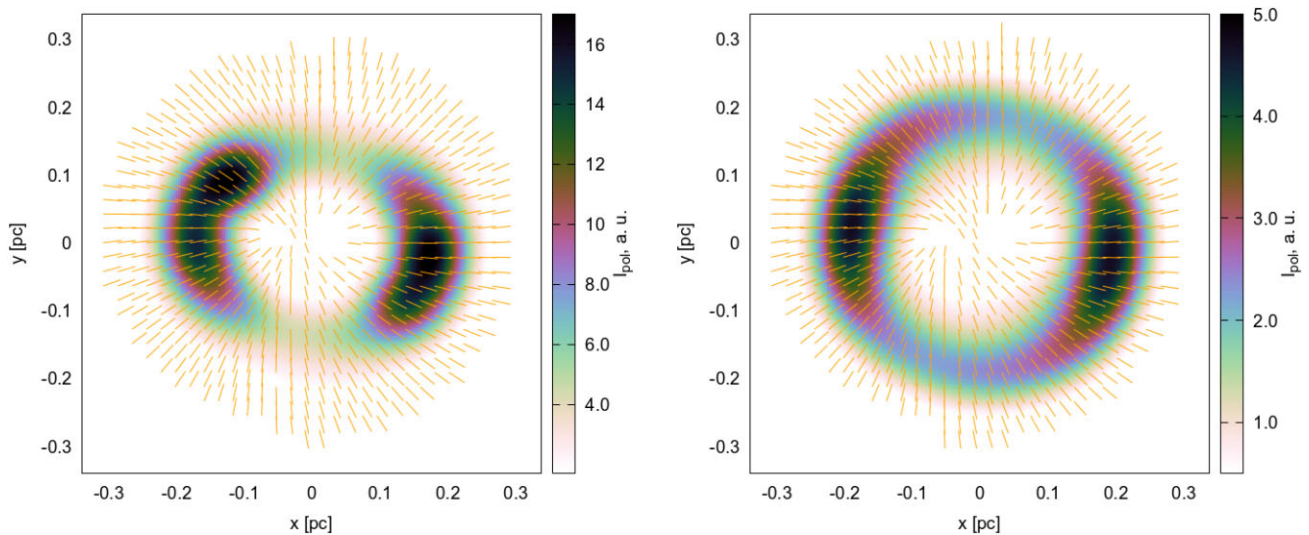

Figure 5. Polarization images of SN1987A synthesized by our method for HD data from Orlando et al. (2019). I_{pol} is shown by colour. Vectors correspond to the orientation of MF and are proportional to the polarization fraction. Left-hand panel: *alternative A*. Right-hand panel: *alternative B*. Arbitrary units in colour scales are the same on Figs 5 and 6 and are 1/100 of the units for Figs 2 and 3.

The images we derive are shown in Fig. 6. They resemble the observed patterns, even in small-scale details. Namely, (i) the radial directions of the polarization vectors are dominant; (ii) the directions of the vectors over the different parts of the SNR edge are almost the same as in the observational data, even deviations from the radial directions; (iii) the sizes of the polarization vectors over the image approximately matches the observed distribution; (iv) there are two blind spots around the center of the image; (v) the SW–NE direction of the vectors between these two spots is also recovered (it is more clearly visible on right-hand panel of Fig. 6).

4.2 East–west asymmetry

The observed east–west asymmetry in the radio images of SN1987A (Cendes et al. 2018; Zanardo et al. 2018) may have different nature. Since the synchrotron emission is proportional to the product $\kappa B^{\alpha + 1}$, the asymmetry should arise mainly from the gradient of MF or density (Gaensler et al. 1997). Radio images of SNRs are more sensitive to the gradient of MF (Orlando et al. 2007). In fact, to be solely responsible for the exponential factor in emissivity, the length-scale of the non-uniformity for the ambient density has to be $H = 0.5$ pc while the length-scale for the MF
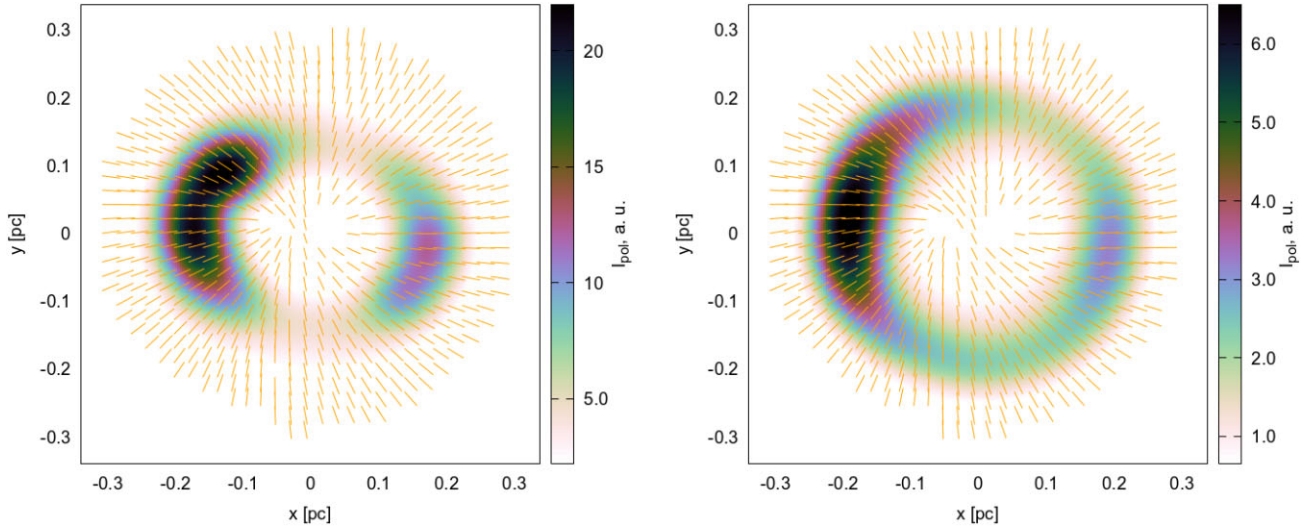
Figure 6. The same as Fig. 5 with gradient of emissivity added.

strength could be larger, $H(\alpha + 1) = 0.85\,\mathrm{pc}$, i.e. the gradient smaller.

X-ray images (Frank et al. 2016) also exhibit east–west asymmetry. However, the origin of the X-ray asymmetry could differ from the radio asymmetry because of the thermal nature of X-ray emission which is dominated in the last decade by the dense structures of ring and clumps (Orlando et al. 2015). Really, the radio emission is proportional to the density while the thermal X-rays to the density squared. What is also important that the asymmetry in X-rays is inverted: Eastern part of SNR was brighter till the year 2007 but then the western part is dominant (fig. 6 in Frank et al. 2016). In the radio band, the eastern part continue to be brighter (Cendes et al. 2018). The brightness inversion in the thermal X-rays, together with the fact that the east side faded first in the optical, may be a sign that the west side of the remnant is denser. If so, the MF gradient, directed to the east, should be stronger (i.e. with smaller H than estimated above) to compensate for the density gradient directed to the west.

Could the dense clumps be (partially?) responsible for such behaviour of the X-ray images? After all, the shock encounters each of them at different times (Fransson et al. 2015). Could the asymmetry in the radio images be also influenced by the clumps? What is dominant in the asymmetry of the radio images: a large-scale gradient of density or of MF? Which MF component, ordered or disordered, is more asymmetric? Could the asymmetry be due to anisotropy of electron injection or acceleration? Might it be due to a non-spherical SN explosion? Expanding with different velocities the parts of the shock may reach dense H II region and equatorial ring earlier at one side than at the other. In order to answer these questions, dedicated studies have to be performed. Analysis may benefit from observational data in different electromagnetic domains which may help to disentangle contributions to the emission from density and MF.

4.3 Radial versus tangential components of magnetic field

4.3.1 Consequences from the model of the Parker spiral

It was demonstrated (Petruk et al. 2021) by 1D MHD simulations that it is unlikely that the radial MF may dominate the tangential one downstream of the forward shock in young SNRs if their strengths

were of the same order in the pre-shock medium. The radial MF component drops faster downstream than the tangential component.

In agreement with this, we have found in this paper that the preferentially radial alignment of the polarization vectors in SN1987A should be due to the dominant radial initial MF around the progenitor.

In our study, we adopted the Parker (1958) model of MF. In the equatorial plane, the ratio between the absolute values of the radial and tangential components in this model varies with a distance and depends on the ratio between the stellar wind speed and the rotation velocity

$$\frac{B_\mathrm{r}}{B_\phi} = \frac{u_\mathrm{w}}{\omega_\mathrm{s}} \frac{1}{r}. \tag{6}$$

The period of magnetic rotation is generally considered the same as for the stellar rotation, $P = 2\pi/\omega_\mathrm{s}$. The two periods may differ if MF is not frozen into the outer layers of a star.

In the model MOD-B1 (Orlando et al. 2019), $u_\mathrm{w} = 500\,\mathrm{km\,s^{-1}}$ and $P = 2 \times 10^4 P_\odot$ with $P_\odot = 27$ days were taken. For these values, the ratio $B_\mathrm{r}/B_\phi = 0.52$ at a distance $r = 0.23\,\mathrm{pc}$ (the radius of SN1987A). Thus, the tangential component is high in the MOD-B1 model.

Our results show that the observed polarization pattern may be reproduced if the radial MF component in the Parker (1958) MF model is dominant on the length-scale of the radius of SN1987A, $B_\mathrm{r} \gg B_\phi$. Numerically, the ratio should be $B_\mathrm{r}/B_\phi \gtrsim 10$ at $r = 0.23\,\mathrm{pc}$. This may be reached if $u_\mathrm{w}/\omega_\mathrm{s}$ in expression (2) is more than ∼20 times larger (and thus A_2 smaller) than in the MOD-B1 model. This factor 20 is a sort of a lower limit (corresponding upper limit to A_2 is ∼4×10^9 G cm): smaller value of the factor or larger SNR radius will cause more tangential polarization pattern.[2]

Our images reported above were synthesized for the factor 40. Though the factor 20 results in the synthesized image, which, in general, is similar to the observed one, the value 40 provides more

---

[2] The ratio $u_\mathrm{w}/\omega_\mathrm{s}$ yields the radius in the equatorial plane r_0 where the tangential velocity due to the rotation $\omega_\mathrm{s} r_0$ equals to the radial velocity of the wind u_w. At this radius, $B_\mathrm{r} = B_\phi$. The tangential MF component gets progressively higher than the radial one for distances $> r_0$ and, at later times (when SNR radius becomes larger) the SNR feels mostly the B_ϕ component. For reference, $r_0 = 0.12\,\mathrm{pc}$ in the MOD-B1 model and should be larger than 2.4 pc to be consistent with the radial polarization in our model of SN1987A.

accurate correspondence to observations on the smaller scales. If we divide the factor 40 evenly between the wind and rotation, we come to the numbers $u_w = 3200\,\mathrm{km\,s^{-1}}$ and $P = 9400\,\mathrm{yr}$. Such wind velocity for the progenitor of SN1987A (B3 class star with temperature $16\,\mathrm{kK}$) is acceptable. For stars in the main sequence, it varies from $\sim 10\,\mathrm{km\,s^{-1}}$ for cool to $\sim 3000\,\mathrm{km\,s^{-1}}$ for hot luminous stars (Johnstone et al. 2015). It could be in the range $2500-3500\,\mathrm{km\,s^{-1}}$ for massive stars with temperatures $25-40\,\mathrm{kK}$ (Vink 2018, their fig. 2). In contrast, the rotational period $\sim 10^5 P_\odot$ is out of the values reported in the literature. Typically measured periods range from hours to months for stars of different types. There are Ap stars with determined periods of $10-30\,\mathrm{yr}$ (e.g. Mathys et al. 2019; Mathys, Kurtz & Holdsworth 2022) and $\sim 100\,\mathrm{yr}$ with expectation that periods may reach several centuries (Mathys 2017). As stated by Mathys et al. (2019), our knowledge about long periods of star rotation is quite incomplete. This is in particular due to difficulties in determination of variations on such long time-scales and in measurement of the radial velocity component $v\sin i$ below the microturbulent velocity $\sim 20\,\mathrm{km\,s^{-1}}$ (Sundqvist et al. 2013; Markova et al. 2014). For the sake of comparison, the values needed to be derived in observations are $v\sin i = 0.004 P_*^{-1}\,\mathrm{km\,s^{-1}}$ for periods P_* in units of $1000\,\mathrm{yr}$ and stars with the radius and inclination as in the progenitor of SN1987A.

4.3.2 On the rotation of the SN1987A progenitor

The spectra of Sanduleak $-69\,202$ observed a decade before the explosion (Walborn et al. 1989) suggest that the rotational velocity of this star may not be above $100\,\mathrm{km\,s^{-1}}$ (Parthasarathy et al. 2006). So, the rotational period exceeded 2 weeks prior the explosion. It is unknown, however, to what degree it was larger than few weeks.

The slow rotation of the progenitor star of SN 1987A suggested by this study seems to be in tension with current models of the progenitor. One of the reasons why the single-star progenitor model for SN1987A was rejected is a low rotation rate of a single star (Podsiadlowski 1992). The binary merger model was introduced because the rotation helps an evolutionary model for an SN1987A progenitor to pass a series of necessary tests (Chevalier & Soker 1989; Podsiadlowski 1992; Morris & Podsiadlowski 2007).

The ambient medium where SN1987A expands is axisymmetric and strongly asymmetric in respect to the polar angle. The HD model (Morris & Podsiadlowski 2006, 2007, 2009) adopts binary merger, the red Supergiant (RSG), the blue Supergiant (BSG) sequence with strong rotation in order to explain such structure. The MHD model (Washimi, Shibata & Mori 1996; Tanaka & Washimi 2002) explains the asymmetry by an evolutionary sequence of the RSG and BSG winds controlled by a strong toroidal MF and also needs a strong rotation as an origin of such MF.

Instead, the model of the Parker spiral for the pre-explosion ambient MF configuration together with the radial polarization pattern in SN1987A imply a slow rotation of the MF around the progenitor star. At this point, we may mention the two possibilities when the strong rotation and the radial MF may coexist in the evolutionary scenario for the progenitor.

First, one might imagine a separation of the ambient MF from a stellar rotator in *space*, by decoupling the spinning core from the outer layers of the star which have low angular momentum (M.A.Aloy 2022, private communication). We cannot say anything more at this point because the core-envelope rotational coupling in stars is an open problem (e.g. Steinle & Kesden 2021). Some authors support effective decoupling in terms of rotation between the stellar interior and the outer layers in the isolated single post-main-sequence stars (Hurley, Pols & Tout 2000). Others, considering binary systems, disfavor models with mild rotational coupling (Belczynski et al. 2020). Alternatively, deviations from ideal MHD conditions may split the MF and star rotations. MF may not be frozen in the stellar material if there is a non-zero resistivity. In such circumstances, their periods of rotation may differ.

In the second scenario, the radial ambient MF may be separated from the rotating star in *time*. The ambient MF at some distance from the star reflects the rotation of that star at the time when this 'portion' of the field was produced. So, when did the star have rotation velocity that low to produce MF configuration with a negligible toroidal MF component? The polarization map we observe now is the result of the shock interaction with the H II region, which is believed to be a material of the wind during the RSG stage of the star evolution. Therefore, the slow rotation might be a feature of this phase. In fact, it is known from the angular-momentum conservation that when the radius of a main-sequence star increases to a supergiant one, the angular rotation of the star decreases considerably (Chevalier & Soker 1989).

The slow-merger scenario suggests that the spinning-up time for the merger, common envelope and mass ejection from the merger is short ($\sim 100\,\mathrm{yr}$) comparing to the next RSG stage (few $1000\,\mathrm{yr}$) (Morris & Podsiadlowski 2007; Urushibata et al. 2018). The matter from the merger was ejected in the polar directions (Morris & Podsiadlowski 2007, 2009) and takes a large fraction of the angular momentum away (Urushibata et al. 2018). Therefore, the 'layer' of the ambient medium filled with the material which has the high angular momentum (and thus the tangential MF component) should be rather thin and form polar lobes. As a result, it should be inefficient in modification of the overall polarization pattern of SN1987A which is due to emission from the equatorial H II region.

In the scenario of Morris & Podsiadlowski (2006, 2007, 2009), one of the stars in the initial binary system was already RSG with 'slow' (few $10\,\mathrm{km\,s^{-1}}$) spherically symmetric wind. The wind of RSG after the merger phase was within the equatorial polar angles and served as a channel for losing the remaining angular momentum. At the next BSG stage, the wind was spherically symmetric (i.e. non-rotating) and 'fast' (few $100\,\mathrm{km\,s^{-1}}$) in this model. In other words, there is a change in the regime of the matter outflow from the post-merger RSG to BSG.[3] Namely, the rotation of RSG slows down to the end of RSG epoch and then the material of RSG wind is blown out by the non-rotating BSG wind. The inner boundary of the H II region corresponds to the transition from the dense RSG wind to the thin BSG wind. Therefore, the MF close to the inner boundary of the H II region (where the SNR shock is propagating now and where the synchrotron emission arises) was originated from a star which was a slow rotator at that time. Afterwards, the matter with this MF was pushed away by the BSG wind to the present-day location. In this process, the angular momentum conservation reduces the (already low) tangential MF even more.

One might suggest a hypothetical way to put limitations on the rotation rate of the star at the time when the equatorial ring was created. This dense equatorial ring is believed to be ejected at the RGB phase (Blondin & Lundqvist 1993; Morris & Podsiadlowski 2009). The location of the ring within the H II region (Chevalier & Dwarkadas 1995) supports this hypothesis. There are detailed *Hubble Space Telescope* observations of the ring with the dense blobs resolved (e.g. Fransson et al. 2015; Larsson et al. 2019). The small

---

[3]Instead, the Parker MF model assumes the steady wind and rotation.

changes in their radial locations are detected (fig. 3 in Fransson et al. 2015). It could be important to derive limitations on the rotational period at the RSG phase by looking for azimuth shifts of the bright blobs in the equatorial ring. However, the detected radial motion of clumps ($\Delta R \sim 0.01$ arcsec on the time-scale ~ 1 yr) are due to velocities of order of few $100 \, \mathrm{km \, s^{-1}}$. The azimuth velocity at the radius of the equatorial ring ($r_{rg} = 0.18$ pc) would be just $R_{rsg}/r_{rg} \sim 3 \times 10^{-5}$ of the equatorial rotational velocity of the progenitor at the time when the ring was created (we have taken $R_{rsg} = 240 R_\odot$ as the RSG radius for this estimate). Therefore, the azimuth shifts in the ring may be noticeable on ~ 10 yr time scale only if the initial equatorial velocity was of the order of the light speed that is impossible. We may interpret this in the other way. Since the equatorial velocity of the star was smaller than the critical velocity ($\sim 100 \, \mathrm{km \, s^{-1}}$) at the end of the RSG phase (and we are unable to detect today the azimuth speed in the ring), the tangential component of frozen-in MF may not be detected at the present radius of SN1987A.

4.3.3 Radial polarization patterns in young SNRs

The preferentially radial orientation of the polarization vectors seems to be common feature for young SNRs while the tangential vectors happen mostly in evolved SNRs (Dickel & Milne 1976; Dubner & Giacani 2015). Radial polarization is observed in young SNRs with progenitors of different nature, for example, SN1987A was peculiar type II SN, Cas A the type IIb, SN1006 the type Ia. Different causes may act in different SNRs but the common property stimulates thoughts about a universal reason for the property. A number of hypotheses for the radial polarization patterns have been suggested.

Our results reveal that the small tangential MF component in SN1987A could be a property of the progenitor star at some stage of its evolution.

The origin of the radial polarization patterns due to the Rayleigh–Taylor (RT) instabilities was considered by Jun & Norman (1996a), Jun & Norman (1996b). The authors concluded in the latter paper that RT instability may be responsible for the radially-oriented MF lines in the mixing region around the contact discontinuity. In our 3D simulations (Orlando et al. 2019), the RT instabilities are well developed at the border between the swept-up ambient material and the stellar ejecta. As an example, one quite prominent 'finger' is shown in Fig. 7. It is elongated along the SNR radius. MF is hydrodynamically amplified up to 50 times the pre-shock value (yellow colour) and has radial direction (MF lines are almost along the radius) there. However, as we see from Fig. 2 and 3, the RT instabilities are ineffective to provide the dominant radial orientation of the polarization pattern in MOD-B1 MHD model because their 'filling factor' is not enough to dominate the polarization pattern.[4] This is in agreement with the earlier findings, namely, with the low amount of MF amplified by such instabilities (Jun & Norman 1996a).

Our approach assumes that the polarization pattern arises in SN1987A due to a dominant contribution from the 'ordered' large-scale MF (including RT instabilities) and not due to the 'disordered'

---

[4]It merits to be noted that we adopted the re-grid technique in 3D MHD simulations in order to follow the SNR evolution over orders of magnitudes in space and time (Orlando et al. 2019). At each regrid, we lost information about features on the smallest length-scales. The grid size, however, is rescaled to just 1.2 times at each re-grid. The small value in 20 per cent has been chosen for regrid in order to keep the small features evolving in our simulations. Therefore, we expect that most of the RT instabilities are preserved in the course of our simulations.
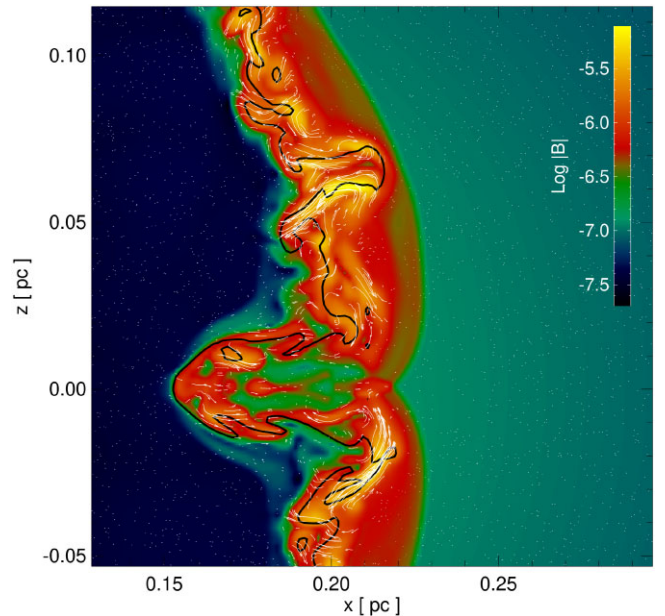
Figure 7. Fragment of a cross-section of MF data cube from MOD-B1 model. Colours show the MF strength in G. The MF lines are white. The contact discontinuity is derived from the tracer of ejecta with the threshold at 0.5 and is shown by the black line. The RT finger is located nearly along the coordinate $z \approx 0.06$ pc. The feature along the coordinate $z = 0$ pc is due to the interaction with the equatorial ring.

MF turbulence which could be excited by accelerated cosmic rays at the smaller scales (we cannot treat it because of numerical limitations imposed by the available spatial resolution). A turbulent MF in SNRs may also be originated by the Richtmyer–Meshkov instability induced at the forward shock by its interaction with the preexisting upstream density perturbations (Inoue et al. 2013). If shock-accelerated cosmic rays or the shock interaction with the large-scale ambient turbulence could amplify preferentially the radial MF component and such a process is able to provide the dominant radial field in the most of emitting volume (like considered by Potter et al. 2014) then the possibility to infer information about the configuration of the pre-SN MF from the polarization observations could be questionable.

Another possibility for the radial polarization is presented by West et al. (2017). It is suggested that the pattern could be due to specific distribution of radio-emitting electrons. If the particles are accelerated preferentially on the parallel portions of the shock then the only radial component of the completely turbulent MF will be highlighted. Such effect requires extremely selective particle acceleration and a dominance of the highly disordered MF over the 'ordered' component.

4.4 Disordered component of magnetic field

As in the observational results, the vectors on our images are proportional to the polarization fraction. Their lengths are similar to those in the observational image. This means that the polarization fraction maps are also similar. However, the values of that fraction in our model are higher than observed because we excluded for simplicity the turbulent MF component from our consideration.

The mean fraction Π of polarized emission from SN1987A at 22 GHz is 2.7 ± 0.3 per cent in the brightest eastern lobe and 3.6 ± 1.5 per cent in the inner part Zanardo et al. (2018). The maximum
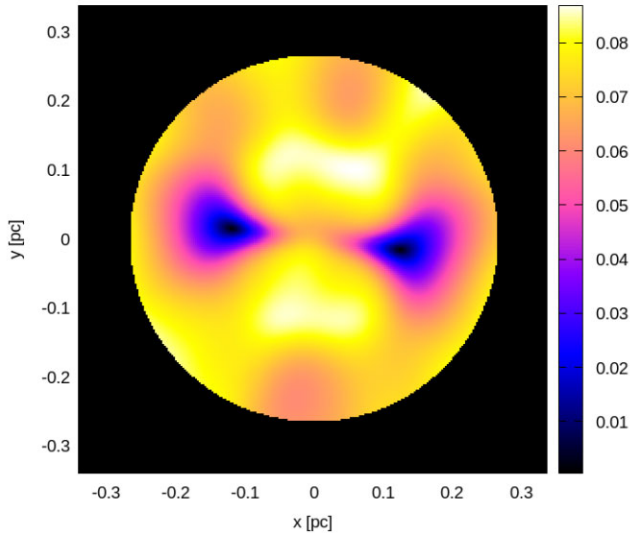
Figure 8. Image for the polarization fraction Π. MOD-B1 model by Orlando et al. ([2019](#)) with the random MF added artificially in each cell with $\delta B/B =$ 1.5. *Alternative B* of the distribution of emitting electrons.

local Π is about 6−8 per cent, as from the sizes of vectors in the observational image.

The polarization fraction decreases in those regions of the SNR projection where MF rapidly changes orientation along the line of sight inside SNR, either due to MHD instabilities or due to turbulent MF. In our 3D model, the instabilities develop and lower the fraction of polarization. In the MOD-B1 data, the fraction varies over the SNR projection from few per cent to about 50 per cent. It is 15–25 per cent in the bright eastern limb. In order to have an idea about the random MF component in SN1987A, we adopt the approach developed in Bandiera & Petruk ([2016](#)) and Petruk et al. ([2017](#)). Namely, we add to each cell the random MF distributed with the spherical Gaussian with the standard deviation δB. To be more specific, we calculate the local Stokes parameters Q and U with formulae (19)–(20) from Petruk et al. ([2017](#)), i.e. multiplying the expressions in the parentheses (which are sensitive to the ratio $\delta B/B$) to the local Q and U which are calculated with the ordered MF which is given by MHD simulations. We keep the ratio $\delta B/B$ the same in the whole volume of SNR and synthesize the polarization maps for MOD-B1 model and different values of this ratio. Note, that since we consider the spherical Gaussian for the random MF orientations, the patterns of the Stokes parameters remain the same (i.e. they are determined by the ordered MF component in this approach). However, the values of Π decrease with increasing $\delta B/B$.

The map of polarization fraction with values of Π similar to those observed is shown in Fig. [8](#). It is produced for the $\delta B/B = 1.5$. Thus, we expect that the disordered and ordered MF components in SN1987A are of the same order.

5 CONCLUSIONS

In this paper, we have modeled the pattern of polarization vectors in SN1987A which resembles the observed one reported by Zanardo et al. ([2018](#)). This was done by using an approximate method for reconstruction of the spatial structure of MF in SN1987A at the age of 30 yr. The method utilizes the numerical 3D HD model of the SN1987A (Orlando et al. [2015](#), [2019](#)), which agrees with temporal and spectral evolution of the remnant in X-rays. We have revealed

some properties of MF and structure of the synchrotron emission in SN1987A which may be used for the future full-scale 3D MHD simulations. Namely, an almost radial ambient MF is needed to reproduce the observations. If the circumstellar MF in the pre-SN era may be described with a Parker spiral, it should be with a negligible tangential component on the length-scale of 0.23 pc, the present-day radius of SN1987A. From the Parker model (which assumes the steady wind and steady rotation), the implication would be either quite slow rotation of the progenitor star and/or the very fast stellar wind before the SN explosion.

We pointed out in Section [4.3](#) that the rotation and wind are not steady in the Morris & Podsiadlowski ([2007](#)) model, namely, (i) the star rotation slowed down toward the end of RSG phase, (ii) the RSG wind bubble was blown up by the spherical BSG wind. Therefore, the azimuth velocity of the material of the RSG wind has considerably decreased due to the conservation of angular momentum, as also the tangential component of frozen-in MF in SN1987A.

We consider two scenarios for the electron injection into acceleration process. Namely, alternative B excludes the possibility for electrons to be injected in the very dense material of the equatorial ring and the clumps. In the alternative A, the injection is considered proportional to the local density also there. We see that the synthesized radio image is more elliptical in alternative A (because the contribution from the ring material is high, Fig. [1](#) left-hand panel) and more circular in the alternative B (because the image is formed by the emitting 'barrel', Fig. [1](#) right-hand panel). The radio emissivity is proportional to $\propto \kappa B^{(s+1)/2}$. Thus, the radio image depends on the relative contributions from the structures of κ (electron injection) and of B. Therefore, the MF strength is not just a normalization for the radio image of SN1987A but serves also as a 'weighting factor' between the alternatives A and B. For example, high MF may be dominant in the formation of the radio image and diminish the role of the dense ring in image for the alternative A. This point has to be taken into account in the future modelling. Being considered together with simulation of the radio light curve, it may put limitations on the MF strength.

An important property of the radio image of SN1987A is the East-West asymmetry in surface brightness (Cendes et al. [2018](#)). This feature is also present in the map of the polarized intensity (Zanardo et al. [2018](#)). Various reasons may produce it, in particular, the gradient of ambient density or MF strength, an asymmetry of SN explosion, the anisotropy in cosmic-ray acceleration or in MF amplification. We have adopted the numerical model of SN1987A with a highly asymmetric explosion (Orlando et al. [2020](#)) and demonstrated that it does not result in the observed radio asymmetry. In order to disentangle other possibilities, dedicated numerical simulations should be performed. It is also important to observe the effect of the internal Faraday rotations. Present observational data are taken at frequency where the internal rotation is ineffective in the modification of the polarization pattern. In order to test alternative hypothesis, polarization observations at longer radio wavelengths would be desirable. In particular, SKA1 could reach 0.4-arcsec resolution at 1.4 GHz.[5] In an unclear situation, we added *the gradient of the radio emissivity* into our model. It is shown that observed east–west contrast in the polarized intensity is comparable to the exponential distribution with the length-scale of order of the remnant diameter.

[5]SKA Technical information. The Telescopes (retrieved on 2022.06.29) http://www.skatelescope.org/wp-content/uploads/2018/08/16231-factsheet-telescopes-v71.pdf

ACKNOWLEDGEMENTS

DATA AVAILABILITY

The data underlying this article will be shared on a reasonable request.

REFERENCES

Abellán F. J. et al., 2017, ApJ, 842, L24

Aloy M. Á., Obergaulinger M., 2021, MNRAS, 500, 4365

Alp D. et al., 2019, ApJ, 882, 22

Arendt R. G., Dwek E., Bouchet P., John Danziger I., Gehrz R. D., Park S., Woodward C. E., 2020, ApJ, 890, 2

Bandiera R., Petruk O., 2016, MNRAS, 459, 178

Belczynski K. et al., 2020, A&A, 636, A104

Blondin J. M., Lundqvist P., 1993, ApJ, 405, 337

Callingham J. R. et al., 2016, MNRAS, 462, 290

Cendes Y., Gaensler B. M., Ng C. Y., Zanardo G., Staveley-Smith L., Tzioumis A. K., 2018, ApJ, 867, 65

Chevalier R. A., Dwarkadas V. V., 1995, ApJ, 452, L45

Chevalier R. A., Soker N., 1989, ApJ, 341, 867

Dickel J. R., Milne D. K., 1976, Aust. J. Phys., 29, 435

Dubner G., Giacani E., 2015, A&A Rev., 23, 3

Falle S. A. E. G., 1975, MNRAS, 172, 55

France K. et al., 2010, Science, 329, 1624

Frank K. A., Zhekov S. A., Park S., McCray R., Dwek E., Burrows D. N., 2016, ApJ, 829, 40

Fransson C. et al., 2015, ApJ, 806, L19

Gaensler B. M., Manchester R. N., Staveley-Smith L., Tzioumis A. K., Reynolds J. E., Kesteven M. J., 1997, ApJ, 479, 845

Greco E. et al., 2021, ApJ, 908, L45

Greco E. et al., 2022, ApJ, 931, 132

Gröningsson P. et al., 2008, A&A, 479, 761

Helder E. A. et al., 2013, ApJ, 764, 11

Hurley J. R., Pols O. R., Tout C. A., 2000, MNRAS, 315, 543

Indebetouw R. et al., 2014, ApJ, 782, L2

Inoue T., Shimoda J., Ohira Y., Yamazaki R., 2013, ApJ, 772, L20

Johnstone C. P., Güdel M., Lüftinger T., Toth G., Brott I., 2015, A&A, 577, A27

Jun B.-I., Norman M. L., 1996a, ApJ, 465, 800

Jun B.-I., Norman M. L., 1996b, ApJ, 472, 245

Kangas T. et al., 2022, MNRAS, 511, 2977

Korobeinikov V., 1964, J. Appl. Mech.Tech. Phys., 4, 113

Kuroda T., Arcones A., Takiwaki T., Kotake K., 2020, ApJ, 896, 102

Larsson J. et al., 2016, ApJ, 833, 147

Larsson J. et al., 2019, ApJ, 886, 147

LeBlanc J. M., Wilson J. R., 1970, ApJ, 161, 541

Maggi P., Haberl F., Sturm R., Dewey D., 2012, A&A, 548, L3

Markova N., Puls J., Simón-Díaz S., Herrero A., Markov H., Langer N., 2014, A&A, 562, A37

Martí-Vidal I., Marcaide J. M., Alberdi A., Guirado J. C., Pérez-Torres M. A., Ros E., 2011, A&A, 526, A142

Mathys G., 2017, A&A, 601, A14

Mathys G., Romanyuk I. I., Hubrig S., Kudryavtsev D. O., Landstreet J. D., Schöller M., Semenko E. A., Yakunin I. A., 2019, A&A, 624, A32

Mathys G., Kurtz D. W., Holdsworth D. L., 2022, A&A, 660, A70

Matsumoto J., Asahina Y., Takiwaki T., Kotake K., Takahashi H. R., 2022, MNRAS, 516, 1752

McCray R., Fransson C., 2016, ARA&A, 54, 19

Miceli M. et al., 2019, Nat. Astron., 3, 236

Morris T., Podsiadlowski P., 2006, MNRAS, 365, 2

Morris T., Podsiadlowski P., 2007, Science, 315, 1103

Morris T., Podsiadlowski P., 2009, MNRAS, 399, 515

Mösta P., Ott C. D., Radice D., Roberts L. F., Schnetter E., Haas R., 2015, Nature, 528, 376

Müller B., Varma V., 2020, MNRAS, 498, L109

Ng C. Y., Gaensler B. M., Staveley-Smith L., Manchester R. N., Kesteven M. J., Ball L., Tzioumis A. K., 2008, ApJ, 684, 481

Ng C. Y., Zanardo G., Potter T. M., Staveley-Smith L., Gaensler B. M., Manchester R. N., Tzioumis A. K., 2013, ApJ, 777, 131

Obergaulinger M., Aloy M. Á., 2020, MNRAS, 492, 4613

Obergaulinger M., Aloy M. Á., 2021, MNRAS, 503, 4942

Obergaulinger M., Just O., Aloy M. A., 2018, J. Phys. G Nucl. Phys., 45, 084001

Ono M., Nagataki S., Ferrand G., Takahashi K., Umeda H., Yoshida T., Orlando S., Miceli M., 2020, ApJ, 888, 111

Orlando S., Bocchino F., Reale F., Peres G., Petruk O., 2007, A&A, 470, 927

Orlando S., Miceli M., Pumo M. L., Bocchino F., 2015, ApJ, 810, 168

Orlando S. et al., 2019, A&A, 622, A73

Orlando S. et al., 2020, A&A, 636, A22

Park S., Zhekov S. A., Burrows D. N., Racusin J. L., Dewey D., McCray R., 2011, ApJ, 733, L35

Parker E. N., 1958, ApJ, 128, 664

Parthasarathy M., Branch D., Baron E., Jeffery D. J., 2006, Bull. Astron. Soc. India, 34, 385

Petruk O., Kuzyo T., Beshley V., 2016, MNRAS, 456, 2343

Petruk O., Bandiera R., Beshley V., Orlando S., Miceli M., 2017, MNRAS, 470, 1156

Petruk O., Kuzyo T., Orlando S., Pohl M., Miceli M., Bocchino F., Beshley V., Brose R., 2018, MNRAS, 479, 4253

Petruk O., Kuzyo T., Orlando S., Pohl M., Brose R., 2021, MNRAS, 505, 755

Podsiadlowski P., 1992, PASP, 104, 717

Potter T. M., Staveley-Smith L., Reville B., Ng C. Y., Bicknell G. V., Sutherland R. S., Wagner A. Y., 2014, ApJ, 794, 174

Ravi A. P., Park S., Zhekov S. A., Miceli M., Orlando S., Frank K. A., Burrows D. N., 2021, ApJ, 922, 140

Reichert M., Obergaulinger M., Aloy M.-A., Gabler M., Arcones A., Thielemann F.-K., 2022, MNRAS, 518, 1557

Sedov L. I., 1959, Similarity and Dimensional Methods in Mechanics. Academic Press Inc., New York

Steinle N., Kesden M., 2021, Phys. Rev. D, 103, 063032

Sugerman B. E. K., Crotts A. P. S., Kunkel W. E., Heathcote S. R., Lawrence S. S., 2005, ApJS, 159, 60

Sun L., Vink J., Chen Y., Zhou P., Prokhorov D., Pühlhofer G., Malyshev D., 2021, ApJ, 916, 41

Sundqvist J. O., Simón-Díaz S., Puls J., Markova N., 2013, A&A, 559, L10

Tanaka T., Washimi H., 2002, Science, 296, 321

Urushibata T., Takahashi K., Umeda H., Yoshida T., 2018, MNRAS, 473, L101

Varma V., Mueller B., Schneider F. R. N., 2022, MNRAS, 518, 3622

Vink J. S., 2018, A&A, 619, A54

Walborn N. R., Prevot M. L., Prevot L., Wamsteker W., Gonzalez R., Gilmozzi R., Fitzpatrick E. L., 1989, A&A, 219, 229

Washimi H., Shibata S., Mori M., 1996, Publ. Astron. Soc. Japan, 48, 23

West J. L., Jaffe T., Ferrand G., Safi-Harb S., Gaensler B. M., 2017, ApJ, 849, L22

Zanardo G. et al., 2010, ApJ, 710, 1515

Zanardo G., Staveley-Smith L., Ng C. Y., Gaensler B. M., Potter T. M., Manchester R. N., Tzioumis A. K., 2013, ApJ, 767, 98

Zanardo G., Staveley-Smith L., Gaensler B. M., Indebetouw R., Ng C. Y., Matsuura M., Tzioumis A. K., 2018, ApJ, 861, L9

This paper has been typeset from a TeX/LaTeX file prepared by the author.